Reduced N/Ni-doped TiO2 Nanotubes Photoanodes for Photoelectrochemical Water Splitting

Journal:	*RSC Advances*
Manuscript ID	RA-ART-10-2015-021805
Article Type:	Paper
Date Submitted by the Author:	19-Oct-2015
Complete List of Authors:	liu, qiang; Institute of Electronic Materials and Technology, School of Materials Science and Engineering, ding, dong; Institute of Electronic Materials and Technology, School of Materials Science and Engineering, Shanghai Jiao Tong University ning, Cong; State Key Laboratory of High Performance Ceramics and Superfine Microstructure, Shanghai Institute of Ceramics, Chinese Academy of Sciences wang, Xue; School of Information Science and Engineering, East China University of Science and Technology
Subject area & keyword:	Nanoanalysis - Analytical < Analytical

Reduced N/Ni-doped TiO_2 Nanotubes Photoanodes for Photoelectrochemical Water Splitting

Qiang liu[a], Dongyan Ding[a, *], Congqin Ning[b], Xuewu Wang[c]

[a] Institute of Electronic Materials and Technology, School of Materials Science and Engineering, Shanghai Jiao Tong University, Shanghai 200240, China.

[b] State Key Laboratory of High Performance Ceramics and Superfine Microstructure, Shanghai Institute of Ceramics, Chinese Academy of Sciences, Shanghai 200050, China.

[c] School of Information Science and Engineering, East China University of Science and Technology, Shanghai 200237, China.

* E-Mail: dyding@sjtu.edu.cn

Abstract

This work reports the facile synthesis of reduced N/Ni-doped TiO_2 nanotubes photoanodes and its photocatalytic activity application. The obtained photoanodes were characterized by scanning electron microscope (SEM), Raman spectrum (Raman), X-ray photoelectron spectroscopy (XPS) and diffuse reflectance absorption spectra. The narrowed band gap of TiO_2 due to the doping of N and Ni elements could enhance the light absorption effectively. The $NaBH_4$ reduction process resulted in the formation of oxygen vacancies in photoanodes. The electrochemical characterization revealed that photo-induced carriers were more efficient charge separation and transportation in reduced N/Ni-doped TiO_2 nanotubes photoanodes. The highest photocurrent density obtained from reduced N/Ni-doped TiO_2 nanotubes photoanodes was 2.52 mA/cm^2 at 0 V vs. Ag/AgCl in 1M KOH solution, which was about five times as high as that obtained from undoped TiO_2.

Keywords: Photoanodes, N/Ni-dopedTiO_2, Reduction, $NaBH_4$, Photoelectrochemical Water Splitting;

1. Introduction

Titanium dioxide (TiO_2) is expected to be an efficient photocatalyst since Fujishima and Honda reported on photoelectrochemical (PEC) water splitting at semiconductor electrodes in 1972 [1-5]. However, TiO_2 materials cannot efficiently utilize the visible light of solar energy due to its comparably large band gap (e.g., 3.2 eV for anatase; 3.0 eV for rutile) and short diffusion paths of charge carriers [6-8]. It is well known that doping modify is an effective method to enhance the photocatalytic activity of titanium dioxide. Many metal ion (Fe, Mo, Cr, Nb, Zr, Mn and Ni) and non-metal ion (C, N, S and F) have been used to dope TiO_2 to change its physical and chemical properties [9-14].

Aligned one-dimensional (1D) nanostructure arrays such as nanorods, nanowires and nanotubes are potential blocks for PEC water splitting because of their unique advantages [15-17]. To fabricate 1D elements doped TiO_2 nanotubes photoanodes had attracted wide attention. This kind element doped TiO_2 nanotubes photocatalyst could take advantage of 1D nanotubes to enhance electron transport rates and increase surface area and enhance electron conductivity for improved photocurrent harvest efficiencies [18, 19]. More importantly, the band gap of TiO_2 could be narrowed because of the incorporation of impurity elements and then the absorption of visible light could also be improved. Recently, Allam et al. fabricated Nb/Zr-doped TiO_2 and Mo/Ni-doped TiO_2 nanotube photoanodes via the anodization of titanium alloys for PEC water-splitting [20, 21]. Mor et al. reported the formation of Fe-doped TiO_2 mixed oxide nanotubes photoanodes to enhance PEC water splitting performance [22]. Schmuki group studied the photocatalytic influence of different Nb contents TiO_2 nanotubes photoanodes under visible light on PEC water splitting [23].

In recent years, oxygen vacancies (V_O) in metal oxides (ZnO, WO_3 and Fe_2O_3) have been extensively investigated through both experimental characterizations and theoretical calculations [24-26]. Oxygen vacancies can act as important absorption and active sites for photocatalysis, which could strongly influence the reactivity of metal oxides [27, 28]. Additionally, oxygen vacancies are believed to provide trapping sites for photo-generated carriers and prevent them from rapid recombination [29].

$NaBH_4$ was widely used as reagent due to its high reducing ability, which could promote the formation of oxygen vacancies in metal oxide. To date, rare works have been reported on the photocatalytic activity of N/Ni-dopedTiO_2 nanotubes photoanodes after $NaBH_4$ reduction treatment. This paper describes the synthesis and photocatalytic activity of reduced N/Ni-dopedTiO_2 nanotubes photoanodes. The photocurrent density of reduced N/Ni-codopedTiO_2 nanotubes photoanodes was 2.52 mA/cm^2 at 0 V vs. Ag/AgCl, which exhibited a remarkable improvement compared to that of undoped TiO_2. Experimental characterizations and theoretical calculations were used to investigate the photocatalytic mechanism of different photoanodes.

2. Experimental section

2.1 Fabrication of reduced N/Ni-doped TiO_2 Nanotubes Phtoanodes

Prior to anodization, Ti50Ni alloy samples (2.0 cm ×1.0 cm × 1mm) were ultrasonically cleaned with acetone followed by a deionized (DI) water rinse. Finally, these samples were dried in N_2 stream for 5 min. The anodization was performed using a two electrode electrochemical system with the prepared Ti50Ni alloys samples as the working electrode and platinum foil as the counter electrode. The anodization was conducted at 35 V for 140 min in 5% ethylene glycol/glycerol containing 0.2 M NH_4F and 0.25 M $(NH_4)_2SO_4$ solution. The temperature of the anodization bath was about 30℃. After anodization, the as-anodized Ni-dopedTiO_2 nanotubes were cleaned with DI water to remove the organic solution followed with N_2 stream drying and then the as-anodized samples were dipped in 1M $NH_3{\cdot}H_2O$ solution for 72 hours to obtain amorphous N/Ni-doped TiO_2 samples. The amorphous N/Ni-doped TiO_2 samples were annealed at 550 °C under air atmosphere for 2 hours. Finally, the annealed N/Ni-doped TiO_2 nanotubes arrays were immersed in 0.3 M $NaBH_4$ for 1hour at room temperature followed by rinsing with water and N_2 stream drying. For reference, the undoped TiO_2 nanotubes photoanodes were fabricated via the anodization of Ti sheets followed annealed at 550 °C for 2 hours under air atmosphere.

2.2 Characterization

Microstructure observations were conducted with a field emission scanning electron microscope (FEI SIRION 200, USA). Raman microscope system (Bruker Opties SENTERRA) with argon ion laser (532 nm) and X-ray photoelectron spectroscopy (XPS; ESCALAB 250, UK) equipped with monochromated Al K_a radiation were used to characterize to chemical states and phase structure of photoanodes. The binding energy was calibrated using the C 1s photoelectron peak at 284.6 eV as reference. The diffuse reflectance absorption spectra of different photoanodes were recorded with UV-Vis spectrophotometer (Perkin Elmer Inc., Lambda 750S, USA) over the range from 300 nm to 800 nm. The PEC properties of different photoanodes were investigated using a three electrode system with a platinum foil as the counter electrode, nanotubes photoanodes as working electrode and Ag/AgCl as the reference electrode, respectively. A 150 W Xe lamp used as light source and the intensity of light illumination was controlled at 100 mW/cm^2. Electrochemical impedance spectroscopy (EIS) of different photoanodes were measured by a scanning potentiostat (CHI Instruments, model CHI660C) with the frequency range from 0.1Hz to 100 KHz. Mott-Schottky plots were generated from capacitance obtained from the EIS spectra at each potential with a frequency of 1000 Hz.

2.3 Calculation of Electronic Structures of different Photoanodes

Density functional theory (DFT) calculations were performed using Cambridge Serial Total Energy Package (CASTEP) code based on the first-principles. The Perdew-Burke-Ernzerhof (PBE) parameterization of generalized gradient approximation (GGA) was adopted to describe the exchange and correlation potential. The cut-off energy for the plane wave expansion was 340 eV. The 3× 2 × 1 ($Ti_{12}O_{24}$) rutile TiO_2 supercells were used to construct a series of TiO_2 systems. The nickel atom, nitrogen atom and oxygen vacancies were doped into rutile TiO_2 supercells to investigate the reduced N/Ni-doped TiO_2. Two nickel atoms and a nitrogen atom substituted for titaniums atom and oxygen atom, respectively. The atomic percentage of the nickel atom and nitrogen atom was 5.56 at.% and 2.78 at.%, respectively. In addition, an oxygen vacancy also was exhibited by the deficiency of oxygen atom in models. In order to make the most stable model, lowest energy substituted position for nickel atom and nitrogen atom should be optimized. The geometry optimization was carried out until all components of the residual forces were less than 10^{-3} eV $Å^{-1}$ and the convergence threshold of the self-consistent energy error was 10^{-5} eV/atom. The *k*-point value 3× 5 × 8 was adopted in the whole Brillouin zone. The optimized structures were used to investigate the electronic structures of different photoanodes.

3. Result and discussions

Fig.1 shows SEM images of different photoanodes. It is clearly seen that uniform Ni-doped TiO_2 nanotube arrays were vertically arranged on the surface of Ti-Ni alloys substrates (Fig.1a). The average inner diameter and length of the Ni-doped TiO_2 nanotubes was 40 nm and 460 nm, respectively. The Ni-doped TiO_2 still kept uniform nanotube arrays after the chemical treatment process (Fig.1b and c). The current-time relation recorded during the anodization of Ti-Ni alloys substrates at 35 V for 2 hours was shown in Fig. 1d. As reported in previous literatures, the formation of Ni-doped TiO_2 nanotubes also includes a competition between electrochemical etching and chemical dissolution processes.

The phase structure of different photoanodes was investigated with Raman spectra, and the measured spectra were presented in Fig 2. For the undoped TiO_2, the peaks at 143, 196, 397, 449, 517, 609 and 635 cm^{-1} were detected. Obvious difference between the Ni-doped TiO_2 and undoped TiO_2 photoanodes were exhibited.

For the Ni-doped TiO_2 samples, the peaks located at 143, 267, 342, 452, 612 and 707 cm^{-1} were detected. All peaks should correspond to rutile TiO_2 except the peak located at 707 cm^{-1} related to titanate peak [30-32]. After the dipping in $NH_3{\cdot}H_2O$ for 72 hours, the titanate peak at 707 cm^{-1} disappeared and the peaks detected at 267 cm^{-1} and 342 cm^{-1} combined together. For the Raman spectra of reduced N/Ni-doped TiO_2 nanotubes photoanodes, no obvious difference was exhibited compared to that of the N/Ni-doped TiO_2. The results indicated that the phase structure of N/Ni-doped TiO_2 did not present obvious change after $NaBH_4$ reduction treatment.

The surface compositions of different photoanodes were examined by XPS. Fig. 3 shows XPS results obtained from different photoanodes samples. For the undoped TiO_2, two peaks located at 458.4 and 464.2eV, which should ascribed to Ti 2p peaks. For the Ni-doped TiO_2 samples, Ti 2p peaks did not exhibit obviously shift. The results could be attributed to that Ni atom could just replace the Ti atom position in TiO_2 samples and did not form additional bond. The new Ti-O-N bond could form in titanium oxide after N-doping. For reduced N/Ni-doped TiO_2 samples, Ti 2p peaks corresponding to Ti $2p_{3/2}$ and Ti $2p_{1/2}$ photoemission spectra were obtained at 458.2 and 464 eV. Fig 3b shows the Ni 2p spectra of different photoanodes. The Ni 2p signal consisted of two peaks at 855.4 and 872 eV, which should be related to Ni^{+2}. Fig 3c shows the O1s spectra of different photoanodes. For reduced N/Ni-doped TiO_2 samples, the O1s peak located at 529.4 should be ascribed to metal oxides.

For the N/Ni-doped TiO_2 samples and reduced N/Ni-doped TiO_2 samples, the high-resolution XPS spectrum of N1s region was shown in Fig. 3d. The peak of N1s at 399.8 eV should be attributed to the interstitial nitrogen atoms in crystal lattice of as Ti-O-N structural feature [33]. Therefore, we concluded that N element was doped into the Ni-doped TiO_2 nanotube arrays successfully. Sun and co-workers also observed a similar peak [34]. There was no obvious difference for N 1s peaks between N/Ni-doped TiO_2 samples and reduced N/Ni-doped TiO_2 samples. Fig. 3e presents the valence band spectra of reduced N/Ni-doped TiO_2 and undoped TiO_2 photoanodes. The valence band edge was estimated by linear extrapolation of the peaks to the baselines, which derives a band edge position of 1.58 eV for reduced N/Ni-doped TiO_2 and 2.66 eV for undoped TiO_2 below the Fermi energy. The results also demonstrated the effects of element doping and $NaBH_4$ reduction treatment on titanium oxide. The facts that the reduced N/Ni-doped TiO_2 samples exhibited a remarkable increased band edge position (vs. undoped TiO_2) indicated an increase in donor density. XPS experiments were conducted to obtain surface compositions of the reduced N/Ni-doped TiO_2 and N/Ni-doped TiO_2 photoanodes. The results reveal that oxygen atoms ratio on surface of reduced N/Ni-doped TiO_2

photoanodes appeared obviously decrease compared to that on N/Ni-doped TiO_2 photoanodes, indicating that $NaBH_4$ reduction treatment could result in the formation of oxygen vacancies. In addition, the atomic percentage of reduced N/Ni-doped TiO_2 photoanodes was investigated by XPS. The atomic percentages of the Ti, Ni, N and O elements were 26.46 at.%, 5.73at.%, 1.95at.% and 65.67at.%, respectively. The results indicated that an amount of oxygen vacancies existed in reduced N/Ni-doped TiO_2 photoanodes.

Fig. 4 shows UV-Vis diffusion reflectance spectra of different photoanodes. The absorption edge of Ni-doped TiO_2 photoanode exhibited a red-shift compared with the undoped TiO_2. Lin and co-worker reported that Ni 3d states were located in the forbidden gap as impurity levels. The impurities levels can lead to a decrease of the photo excitation energy and induce a signification red-shift of the absorption edge [35]. It is apparent that N/Ni-doped TiO_2 photoanode exhibited an enhanced light absorption compared to Ni-doped TiO_2 photoanode. The enhanced light absorption is related to excitation of electrons from localized N 2p in band gap. The reduced N/Ni-doped TiO_2 samples shows a dramatically light absorption from 400 to 600 nm because of the additional transitions between the different energy levels of oxygen vacancy, Ti^{3+} , valence band and conduction band.

To evaluate the influence of N/Ni-doping and $NaBH_4$ reduced treatment, the photocatalytic activity was characterized through the linear sweep voltammograms of different photoanodes under dark and light irradiation without any kind of filters by a conventional three-electrode configuration with platinum foil as a counter electrode, Ag/AgCl (3M KCl) reference electrode and reduced N/Ni-doped TiO_2 nanotubes photoanodes as working electrode. The potential was swept at a scan rate of 10 mVs^{-1} from -1V to1V. Fig. 5a shows the photocurrent density vs. potential of different photoanodes mearsured at 0 V Ag/AgCl in 1 M KOH solution. For the undoped TiO_2, the photocurrent density was about 0.47 mA/cm^2. With the doping of Ni or N/Ni elements, the photocurrent density of photoanodes was improved. As expected, the photocatalytic activity of reduced N/Ni-doped TiO_2 nanotubes photoanodes was greatly enhanced and exhibited a photocurrent density of 2.52 mA/cm^2 at 0V vs. Ag/AgCl after the $NaBH_4$ reduction treatment, which was approximately 5 times as high as that of the undoped TiO_2.

The solar-to-hydrogen conversion efficiency of different photoanodes was calculated according to the following formula [36]:

$$\eta = I(1.23 - V) / J_{light}$$

where I is the photocurrent density at applied bias voltage, V is the applied bias voltage and J_{light} is the intensity of illustration (100 mW/cm^2). Fig. 5b shows the photoconversion efficiency of different photoanodes. The photoconversion efficiency for the undoped TiO_2 photoanode was about 0.23% at -0.52V vs. Ag/AgCl, while a 0.27% photoconversion efficiency was exhibited for the Ni-doped TiO_2 photoanode at -0.28 V vs. Ag/AgCl. For the N/Ni-doped TiO_2 photoanode, the photoconversion efficiency presented a remarkable improvement due to the N element doping at -0.41V (0.81%). After the $NaBH_4$ reduction treatment, the reduced N/Ni-doped TiO_2 photoanode exhibited an increase of 0.31% at -0.43 V compared to that of the pristine N/Ni-doped TiO_2 photoanodes.

In order to investigate the photocatalytic chemical stability of the reduced N/Ni-doped TiO_2 nanotubes photoanodes, 10 hours irradiation were conducted at 0 V vs. Ag/AgCl in 1 M KOH. As shown in Fig. 5c, the photocurrent density of the reduced N/Ni-doped TiO_2 nanotubes photoanodes almost had no decrease. The reduced N/Ni-doped TiO_2 nanotubes photoanodes could keep high photocatalytic activity for a long time. The impacts of $NaBH_4$ treatment on undoped TiO_2 nanotubes and Ni-doped TiO_2 nanotubes were investigated. The reduced undoped TiO_2 nanotubes and the reduced Ni-doped TiO_2 nanotubes photoanodes also were fabricated through the same method as that of the reduced N/Ni-doped TiO_2 photoanodes. Fig.5d shows photocurrent density vs. time scans for the different photoanode measured at 0 V vs. Ag/AgCl. As shown in Fig.5d, the photocurrent density of reduced undoped TiO_2 nanotubes and reduced Ni-doped TiO_2 were 1.2 mA/cm^2 and 1.84 mA/cm^2, respectively. The results indicated that $NaBH_4$ treatment could enhance the photocatalytic activity of TiO_2-based nanotubes photoanodes. Furthermore, the photocatalytic impact of the N-doping on undoped TiO_2 nanotube structures fabricated through the reported method also was investigated in the manuscript. As shown in Fig. 5d, the photocurrent density of N-doped TiO_2 nanotubes photoanodes was 0.68 mA/cm^2. N-doping also could improve the photocatalytic performance of undoped TiO_2.

Accorrding to the above discussion, the reduced N/Ni-doped TiO_2 photoanodes exhibited the higher performance photocatalytic activity, which should be attributed to many factors. Firstly, the N/Ni-doping could narrow the band gap of TiO_2 and enhance the optical absorption. It is well known that $NaBH_4$ is widely used as reducing reagent due to its high reduction ability. It could reduce Ti^{+4} to Ti^{+3} and give rise to oxygen vacancies in semiconductor photoanodes. Many literatures reported that oxygen vacancies could serve as charge carrier traps as well as adsorption sites and the charge transfer to adsorbed species can prevent photon-generated carrier rapid recombination [27, 28]. Thus, oxygen vacancies created through the $NaBH_4$ reduction treatment should be another factor to improve the photocatalytic activity of titanium oxide photoanodes.

In order to investigate the charge transfer and recombination processes at semiconductor electrolyte interfaces, the EIS of different photoanodes were measured at 0 V vs. Ag/AgCl with frequencies ranging from 100 kHz to 0.1Hz in 1M KOH. Fig. 6 shows the EIS Nynquist plot of different photoanodes. It can be found that the TiO_2 photoanodes presented a smaller value of the arc diameter in the Nyquist plot after Ni and N doping. The results indicated that charge transfer resistance decreased compared to the undoped TiO_2 photoanodes. Furthermore, the charges transfer resistance of the reduced N/Ni-doped TiO_2 photoanodes was smaller than that of others photoanodes reported in this paper. The smaller charge transfer resistance for the photoanodes indicated that an enhanced separation efficiency of photo-generated charge carriers across the interface between the electrolyte and the photoanodes [37]. Therefore, the reduced N/Ni-doped TiO_2 photoanodes were expected to have more efficient charge carrier transfer process. The EIS of reduced N/Ni-doped TiO_2 measured under UV-Vis illustration was shown in the inset Fig. 6. The charge transfer resistance was smaller than that of reduced N/Ni-doped TiO_2 photoanodes without UV-Vis illustration. The results revealed that the reduced N/Ni-doped TiO_2 photoanodes had sensitivity to UV-Vis light and thus the photoanodes were expected excellent photocatalytic performance.

The flat-band potential and donor density of different photoanodes were calculated from the Mott–Schottky equation [18, 38]:

$$1/C^2 = (2/e_0\, \varepsilon\varepsilon_0 N_d)[(V - V_{FB}) - kT/e_0]$$

where e is the electron charge, N_d is the donor density, ε_0 is the permittivity of vacuum, V is the applied bias at the electrode, ε is the dielectric constant of TiO_2 ($\varepsilon = 170$) and k is Boltzmann's constant. The component of the impedance Z'' measured at 1000 Hz allowed to evaluate the capacity as $C = 1/2\pi f Z''$. Fig.7 shows the Mott-Schottky plots of different photoanodes. The $1/C^2$ and the applied potential would exhibit a linear dependence. The intersection with the applied potential axis represents the flat-band potential of different photoanodes (E_{fb}). The detailed flat-band potential of different photoanodes was shown in Table 1. For the undoped TiO_2, the flat-band potential was -0.39 V vs. Ag/AgCl. With the doping of N and Ni elements, the flat-band potential shifted to lower potential compared to that of the undoped TiO_2. Additionally, the flat-band potential of the N/Ni-doped TiO_2 nanotubes photoanodes shifted to -0.81V after $NaBH_4$ reduction process. The lower flat-band potential suggests more efficient charge separation and transportation in reduced N/Ni-doped TiO_2 nanotubes photoanodes. Therefore, the reduced N/Ni-doped TiO_2 photoanodes could present higher photocatalytic activity. All samples show positive slopes in the Mott-Schottky plots, as expected for n-type semiconductors.

The donor density of different photoanodes can be calculated by the following equation:

$$N_d = (2/e_0\,\varepsilon\varepsilon_0)[d(1/C^2)/dV]^{-1}$$

The calculated electron densities of different photoanodes were shown in Table 1. As shown in Table 1, the donor density of undoped TiO_2 increased after the chemical process treatment. The donor density measured from Mott-Schottky analysis did not correspond to impurity concentrations in the photoanodes but only approximates the stoichiometric point defects, which in the case of oxide titanium films can correspond to oxygen-ion vacancies.

The higher donor densities would improve the electrical conductivity and charge transport in semiconductor photoanodes. Furthermore, the Fermi level of the TiO_2 shifts toward the conduction band due to the increased donor densities. The upward shift of the Fermi level can increase the degree of band bending at the semiconductor surface, which promotes the charge separation at the semiconductor electrolyte interface. Therefore, the higher separation and transition efficiency for photon-generated carrier in reduced N/Ni-doped TiO_2 photoanodes was expected [29].

In order to understand the origin of the change in electronic and optical properties of different photoanodes, a series of theoretical models were constructed to mimic the different photoanodes. In the theoretical models, the atomic percentage of the nickel atom, nitrogen atom and 5.56 at.% and 2.78 at.%, which was basically consistent with the experimental results. In addition, an oxygen vacancy also was exhibited by the deficiency of oxygen atom in models. Fig. 8 displays the calculated density of states of different photoanodes. For the undoped TiO_2, the energy band is mainly composed of Ti 3d and O 2p states. The isolated energy state located at forbidden band of the Ni-doped TiO_2 photoanodes, which was led due to Ni 3d orbital. These results were in consistent with previous investigations [35]. The electron in valence band (VB) can be excited to localized impurity states in band gap and subsequently to the concentration band (CB). Thus, the excitation energies should be much smaller than that of the undoped TiO_2. This is the reasons why the Ni-doped TiO_2 exhibited red-shift absorption compared with that of undoped TiO_2. In addition, the valence band maximum had no shift while the conduction band bottom had an obvious decline about 0.3 eV for the Ni-doped TiO_2 and N/Ni-doped TiO_2 samples. As shown in Fig. 8, the conduction band of the reduced N/Ni-doped TiO_2 shifted to lower energy, which should be attributed to partial transition metal atomic (Ti and Ni) d states hybridized with the anion (O, N) 2p states due to the incorporation of oxygen vacancies. The Fermi level of the reduced

N/Ni-doped TiO_2 moved toward conduction band due to the extra electrons from impurity atoms extra transferring, which can increase the degree of band bending at the semiconductor surface, which promotes the charge separation at the semiconductor electrolyte interface. Therefore, the photocatalytic performance of the N/Ni-doped TiO_2 photoanodes could be enhanced because of the incorporation of oxygen vacancies via $NaBH_4$ reduction method. Furthermore, the valance band broadens with the maxing of (N, O) 2p and (Ti, Ni) 3d after the incorporation of oxygen vacancies, which enhances the mobility of photo-generated hole [39, 40]. The higher mobility of photo-generated hole could improve the photocatalytic activity of photoanodes.

Mulliken charge on dopant atoms and adjacent atoms of pure, Ni, N/Ni and reduced N/Ni were summarized in Table 2. The Mulliken charge of Ti atoms in reduced N/Ni-doped TiO_2 (1.23) is lower than that of Ti atoms in pure TiO_2, implying the increase of electron density and enhancement in reducibility of Ti atoms in reduced N/Ni TiO_2. The incorporation of oxygen vacancies leads to more electrons transfer from Ni and Ti atoms to N and O atoms. The 3d state of the Ti^{3+} ion is the highly efficient separation center of photo-generated electrons and holes, which was created due to the incorporation impurity states and the $NaBH_4$ reduced treatment. Thus, the charge separation and transportation in reduced N/Ni-doped TiO_2 nanotubes photoanodes were enhanced effectively, which was the main impact to improve photocatalytic activity.

Conclusions

In summary, the reduced N/Ni-doped TiO_2 nanotubes photoanodes were successfully fabricated through facile chemical treatment process of the Ni-doped TiO_2.The Ni-doped TiO_2 nanotube arrays were fabricated via the anodization of Ti-Ni alloys. The doping of the N and Ni elements could widen the optical absorption range of TiO_2. Oxygen vacancies yielded due to the $NaBH_4$ reduction treatment served as charge carrier traps as well as absorption sites. DFT calculation results revealed that ion doping and $NaBH_4$ reduction process could improve the optical absorption and enhance photon-generated carrier separation and transportation. The maximum photoconversion efficiency of the reduced N/Ni-doped TiO_2 photoanodes was 1.12% at -0.52 V vs. Ag/AgCl. The proposed reduced N/Ni-doped TiO_2 nanotubes photoanodes should serve as a model for facile chemical treatment of titanium oxide for efficient PEC water splitting.

Acknowledgments

This work was supported by Shanghai Pujiang Program (No.07pj14047) and National Natural Science Foundation of China (No.51572170). We thank the contribution from SEM and XPS lab at Instrumental

Analysis Center of SJTU.

References

[1]I. Paramasivam, H. Jha, N. Liu and P. Schmuki, *Small*, 2012, 20, 3073–3103.

[2] W. J. Li, R. Liang, A. M. Hu, Z. H. Huang and Y. N. Zhou, *RSC Adv.*,2014, 4, 36959–36966.

[3] M. Ni, M. K. H. Leung, D.Y. C. Leung, K. Sumathy, *Renew .Susta. Energ. Rev*. 2007, 11, 401–425.

[4] Q. Liu, D. Y. Ding, C. Q. Ning and X.W Wang,*Int. J. Hydrogen Energy*, 2015, 40, 2107–2114.

[5] Y. L. Lee, C. F. Chi and S.Y. Liau, *Chem. Mater*. 2010, 22, 922–927.

[6] L. K. Randeniya E A. B. Murphy and EI. C. Plumb, *J. Mater. Sci*. 2008, 43, 1389–1399.

[7] D. D. Li, P. C. Chang, C.J. Chien and J. G. Lu, *Chem. Mater*. 2010, 22, 5707–5711.

[8] S. Lee, Y. S. Lee, D. H. Kim and J. H. Moon, *ACS Appl. Mater. Interfaces*, 2013, 5, 12526−12532.

[9] V. Etacheri, G.Michlits, M.K. Seery, S. J. Hinder and S. C. Pillai.,*ACS Appl. Mater. Interfaces*, 2013, 5 ,1663−1672.

[10] Q. Liu, D.Y. Ding and C.Q. Ning, *Materials.* 2014, 7, 3263−3275.

[11] L. Jia, D. H. Wang, Y. X. Huang, A.W. Xu and H. Q. Yu, *J. Phys. Chem. C*. 2011,115,11466–11473.

[12] J. Zhang, C. X. Pan, P. F. Fang, J. H. Wei and R. Xiong, *ACS Appl. Mater. Interfaces*, 2010, 2, 1173–1176.

[13] M. E. Kurtoglu, T. Longenbach, K. Sohlberg and Y. Gogotsi, *J. Phys. Chem. C*. 2011, 115, 17392–17399.

[14] Y. F.Tu, S.Y. Huang, J. P. Sang, X. W. Zou, *Mater. Res. Bull*. 2010, 45, 224–229.

[15] S. Hoang, S.W. Guo and C. B. Mullins, *J. Phys. Chem. C.*, 2012,116, 23283−23290.

[16] I. S. Cho, Z. B. Chen, A. J. Forman, D. R. Kim, P. M. Rao, T. F. Jaramillo and X. L. Zheng, *Nano Lett*. 2011, 11, 4978–4984.

[17]N. Lu, H. M. Zhao, J. Y. Li, X. Quan and S. Chen, *Sep. Purif. Technol*. 2008, 62, 668−673.

[18] Q. Liu, D. Y. Ding, C. Q. Ning and X. W. Wang, *Mater. Sci. Eng., B*, 2015,196, 15−22.

[19] N. K. Allam, C. W. Yen, R. D. Near and M. A. El-Sayed, *Energy Environ. Sci.* 2011, 4, 2909−2914.

[20] N. K. Allam, F. Alamgir and M. A. El-Sayed, *ACS Nano*. 2010, 4, 5819−5826.

[21] N. K. Allam, N. M. Deyab and N.A. Ghany, *Phys. Chem. Chem. Phys*. 2013,15, 12274–12282.

[22] G. K. Mor, H. E. Prakasam, O. K. Varghese, S K. hanker and C. A. Grimes, *Nano Lett,* 2007, 7, 2356–2364.

[23]C. Das, P. Roy, M. Yang, H. Jha and P. Schmuki, *Nanoscale*, 2011, 3, 3094–3197.

[24] G. M. Wang, Y. C. Ling, H. Y. Wang, X. Y. Yang, C. C. Wang, Jin Z. Zhang and Yat Li, *Energy Environ.*

Sci., 2012, 5, 6180–6188.

[25] Y. C. Ling, G. M. Wang, J. Reddy, C. C. Wang, Ji. Z. Zhang and Y. Li, *Angew. Chem*. 2012,124, 4150 –4079.

[26]G. M. Wang, Y. C. Ling and Y. Li, *Nanoscale*, 2012, 4, 6682–6691.

[27] X. B. Chen, L. Liu, P. Y. Yu, and S. S. Mao, *Science*, 2011, 331,746–750.

[28] L. Liu, P. Y. Yu, X. B. Chen, S. S. Mao and D. Z. Shen, *Phys. Rev. Lett.*, 2013,111, 065505–065509

[29] Q. Kang, J. Y. Cao, Y. J. Zhang, L. Q. Liu, H. Xu and J.H. Ye, *J. Mater. Chem. A*, 2013,1, 5766–5774.

[30]S. U. Kim, Y. U. Yun, S. H. Hong, C. A. Roberts, K. Routray and I. E. Wachs, *J. Phys. Chem. Lett.* 2010, 1, 130–135.

[31] T. Kasuga, M. Hiramatsu, A. Hoson, Sekino and T. Niihara, K. *Adv. Mater*. 1999, 11, 1307–1312.

[32]C. Ratanatawanate, C. R. Xiong and K. J. Balkus, *ACS Nano*, 2008, 2,1682–1688.

[33] Y. K. Lai, J.Y. Huang, H. F. Zhang, V. P. Subramaniam, Y. X. Tang, D. G. Gong, L. Sundar, L. Sun, Z. Chen and C.J. Lin, *J. Hazard. Mater*. 2010,184, 855–863.

[34] L. Sun, J. H. Cai, Q. Wu, P. Huang, Y. F. Su and C. J. Lin, *Electrochim. Acta*. 2013,108, 525–531.

[35] Y. M. Lin, Z.Y. Jiang, C.Y. Zhu, X.Y. Hu, X. D. Zhang and J. Fan, *Mater. Chem. Phys* 2012,133, 746–750.

[36] W. K. Tae and K. S. Choi, *Science*, 2014, 343,990–996.

[37] H. Cai, Q. Yang, Z. G. Hu, Z. H. Duan, Q. H. You, J. Sun, et al. *Appl. Phys. Lett*. 2014,104, 053114–053121.

[38] S. Palmas, A. M. Polcaro, J. R. Ruiz, A. D. Pozzo, M. Mascia and A. Vacca, *Int. J. Hydrogen Energy*, 2010,35, 6561–6570.

[39] W. M. Shi, Q. F. Chen, Y. Xu, D. Wu and C.F. Huo, *Appl. Surf. Sci.* 2011,257, 3000–3006.

[40] X. P. Han and G. S. Shao, *J. Phys. Chem. C*. 2011, 115, 8274–8282.

Captions

Fig.1 Top and cross view images of different photoanodes (a) as-anodized Ni-doped TiO_2, (b) N/Ni-doped TiO_2, (c) reduced N/Ni-doped TiO_2 and (d) is the anodization current density time relations.

Fig. 2 Raman spectra of different photoanodes.

Fig. 3 XPS obtained from different photoanodes (a) Ti 2p, (b) Ni 2p, (c) O 1s, (d) N1s and (e) valence band.

Fig.4 UV-Vis diffusion reflectance spectra of different photoanodes.

Fig.5(a) Photocurrent density vs potential of different photoanodes in 1 M KOH (b) Corresponding photoconversion efficiency of different photoanodes. (c) Amperometric $I-t$ curve collected at 0 V vs. Ag/AgCl of the reduced N/Ni-doped TiO_2nanotubes photoanode. (d) Photocurrent density vs. time scans for the different photoanode with 0 V vs. Ag/AgCl.

Fig.6 Electrochemical impedance spectroscopy (EIS) Nynquist plot of different photoanodes, inset: the EIS of reduced N/Ni-doped TiO_2 measured under UV-Vis illustration.

Fig. 7 Mott-Schottky plots of different photoanodes with a frequency of 1000Hz in the dark. Inset: magnified Mott-Schotty plot of N/Ni-doped TiO_2 and reduced N/Ni-doped TiO_2 photoanodes.

Fig. 8. (a) The calculated and comparison TDOS of different photoanodes, calculated PDOS of (b) undoped TiO_2, (c) Ni-doped TiO_2,(d) N/Ni-doped TiO_2 and (e) reduced N/Ni-doped TiO_2. The zero point energy is Fermi level.

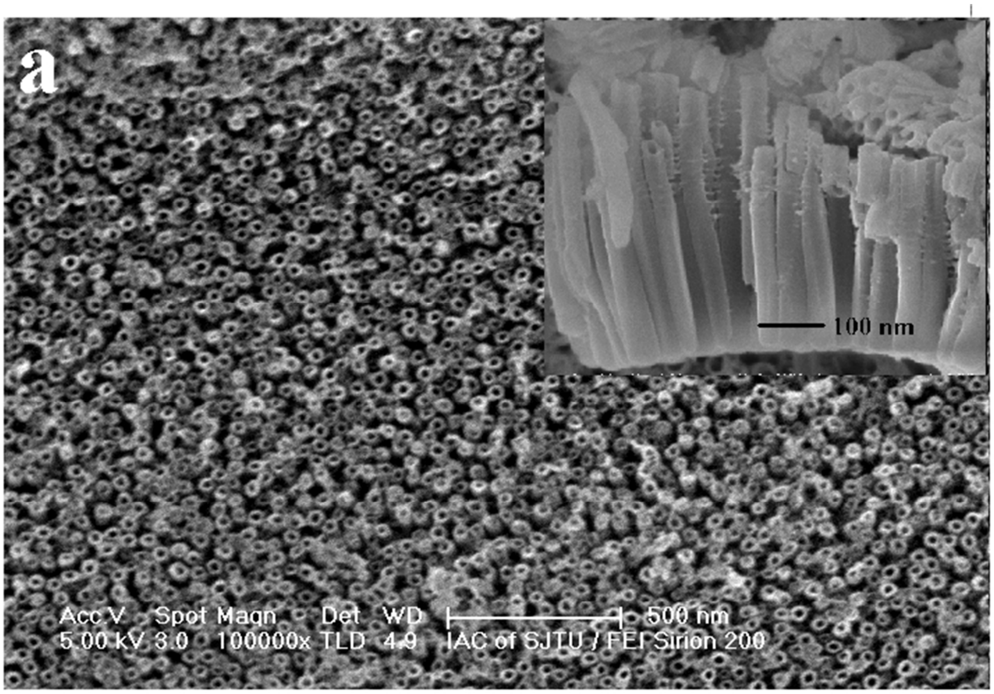

189x132mm (96 x 96 DPI)

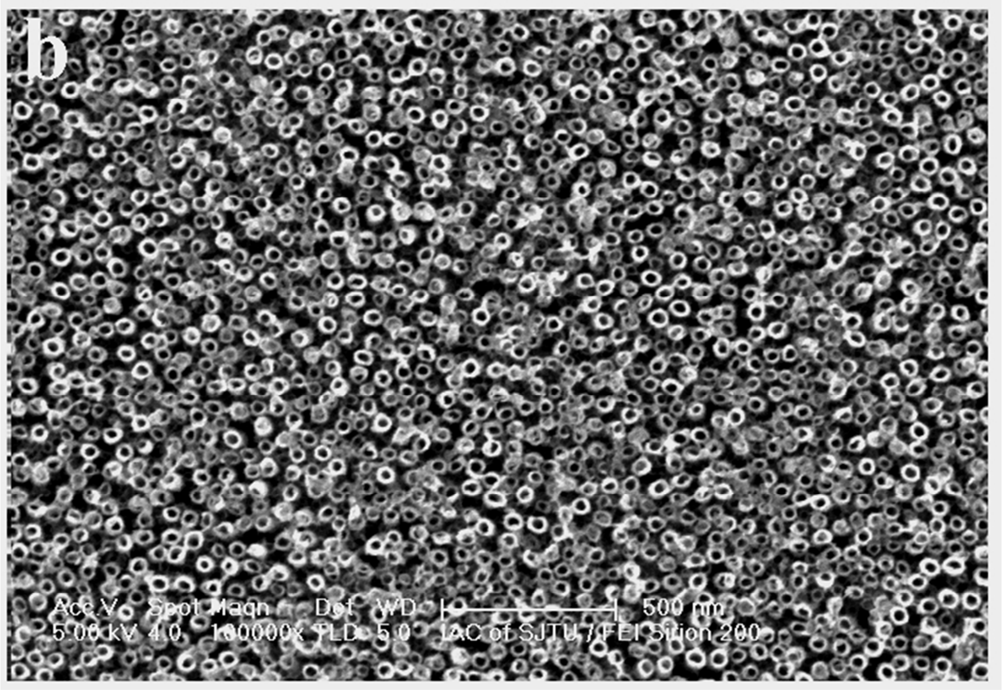

189x130mm (96 x 96 DPI)

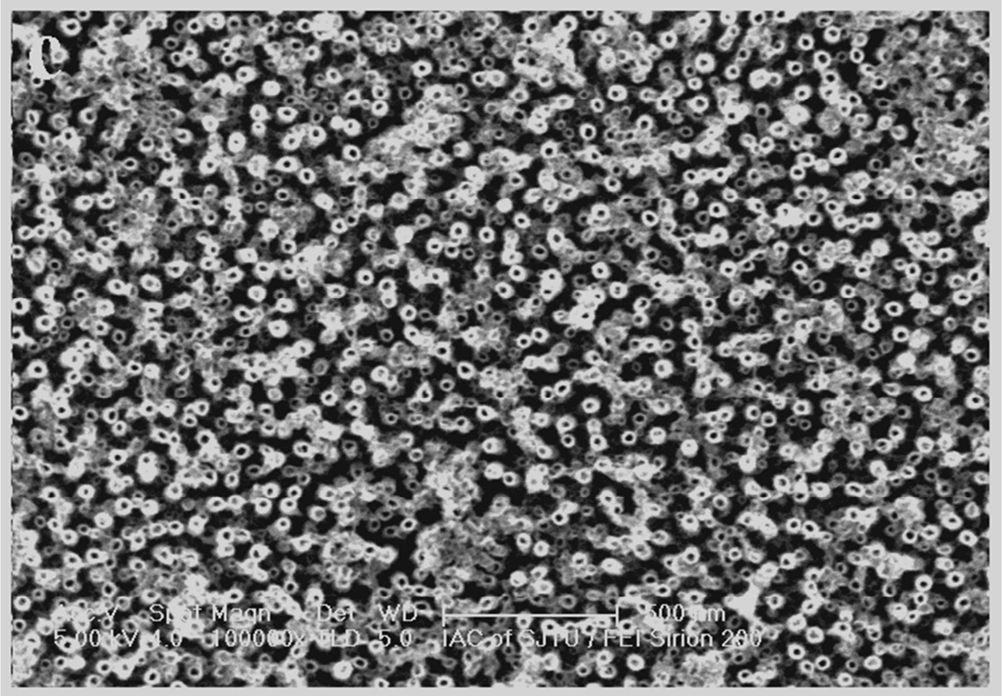

189x131mm (96 x 96 DPI)

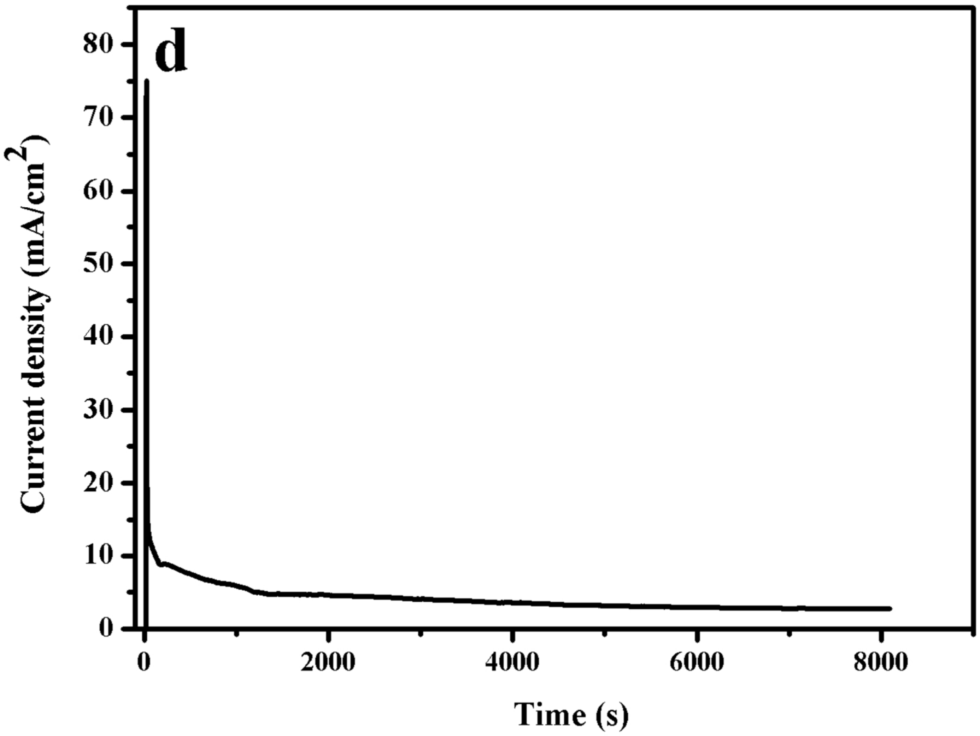

235x176mm (150 x 150 DPI)

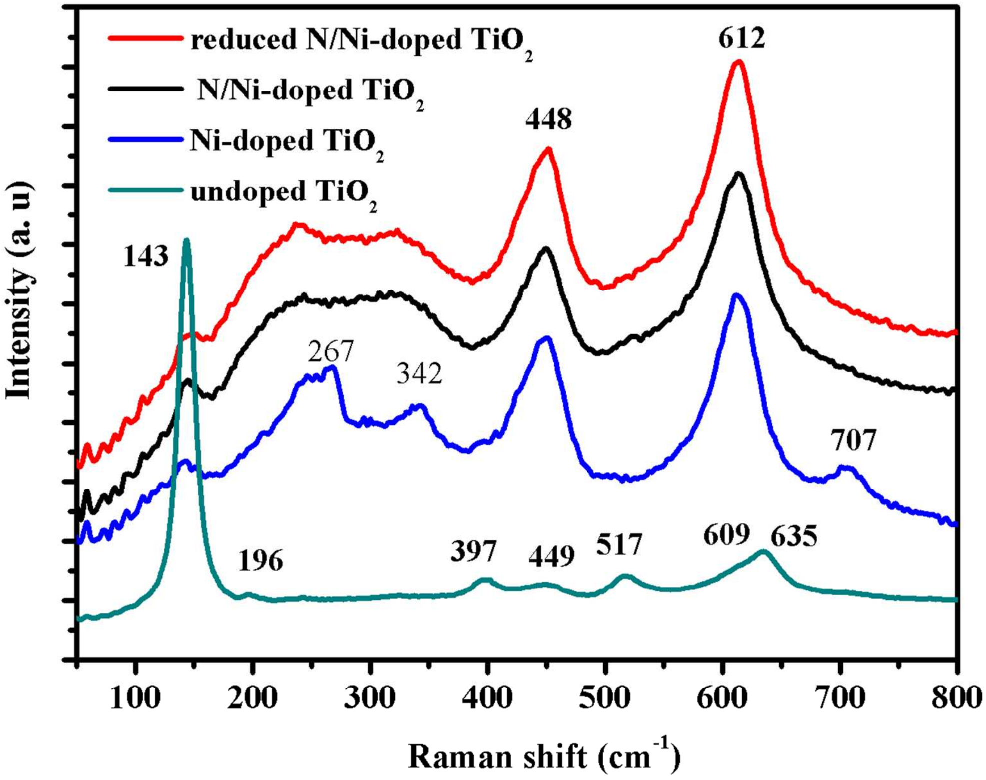

224x177mm (150 x 150 DPI)

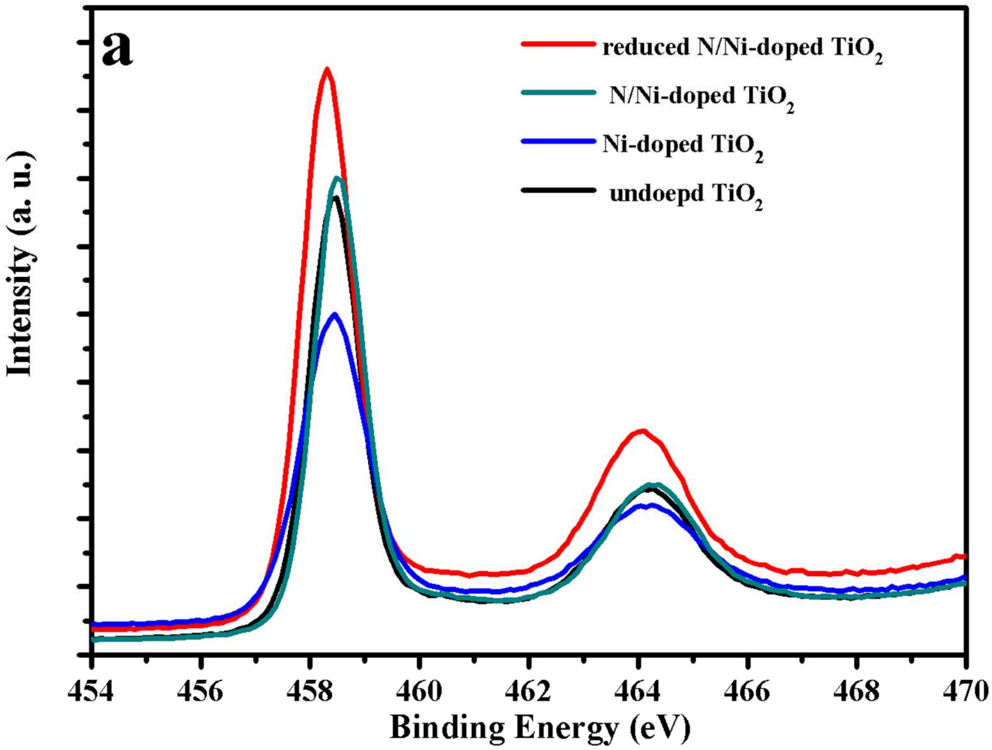

225x172mm (150 x 150 DPI)

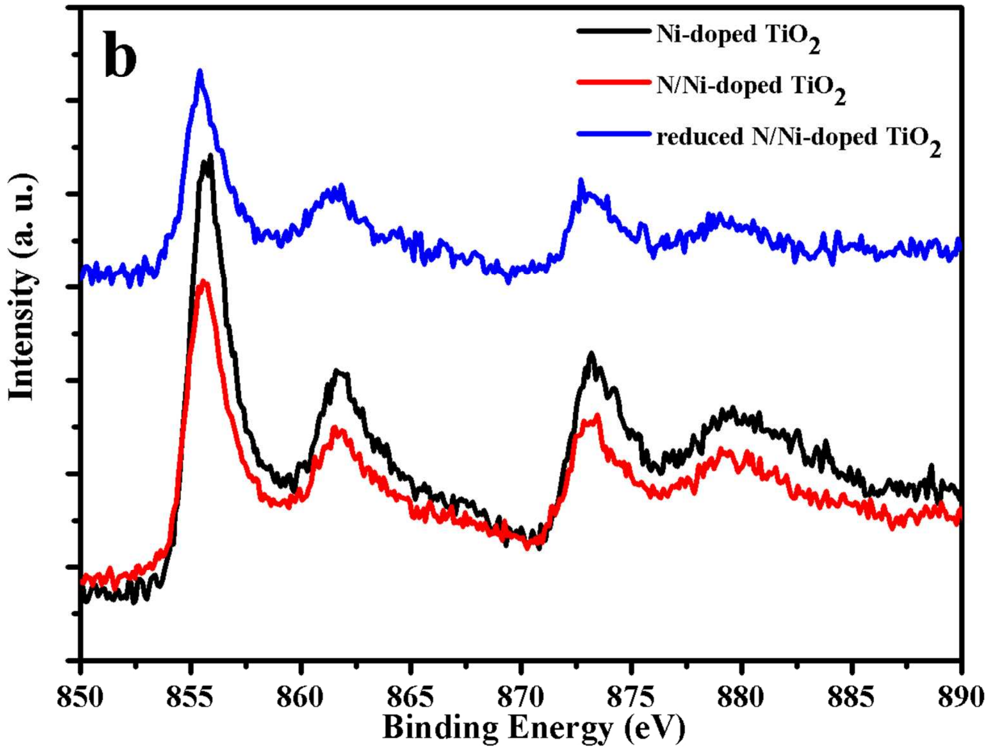

224x176mm (150 x 150 DPI)

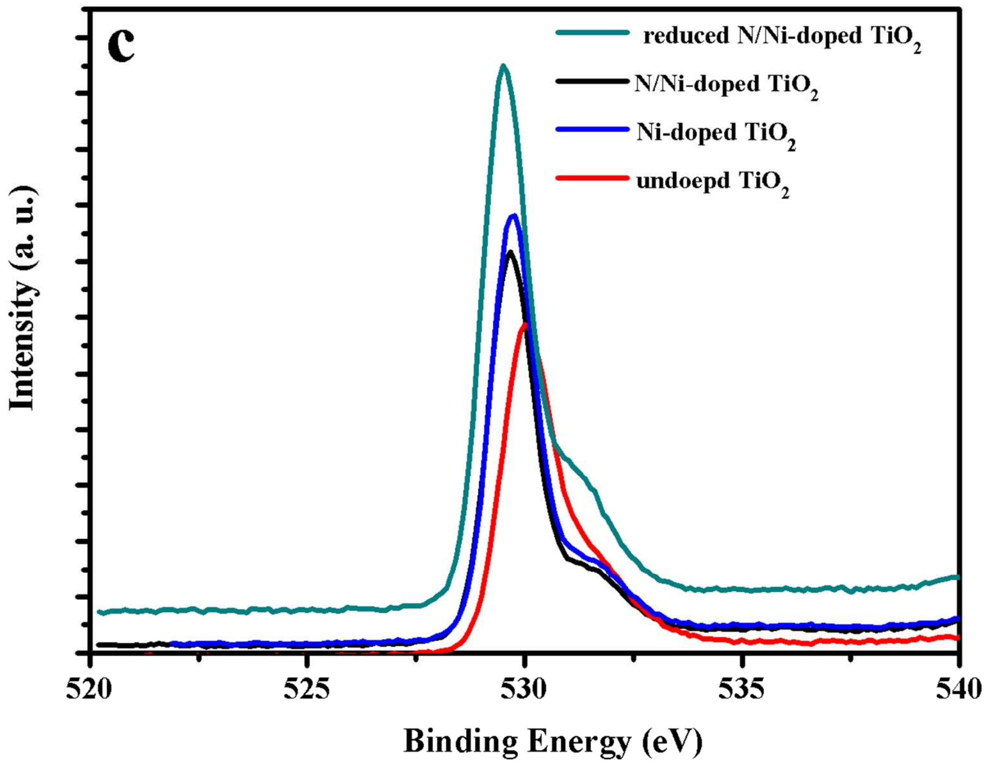

227x176mm (150 x 150 DPI)

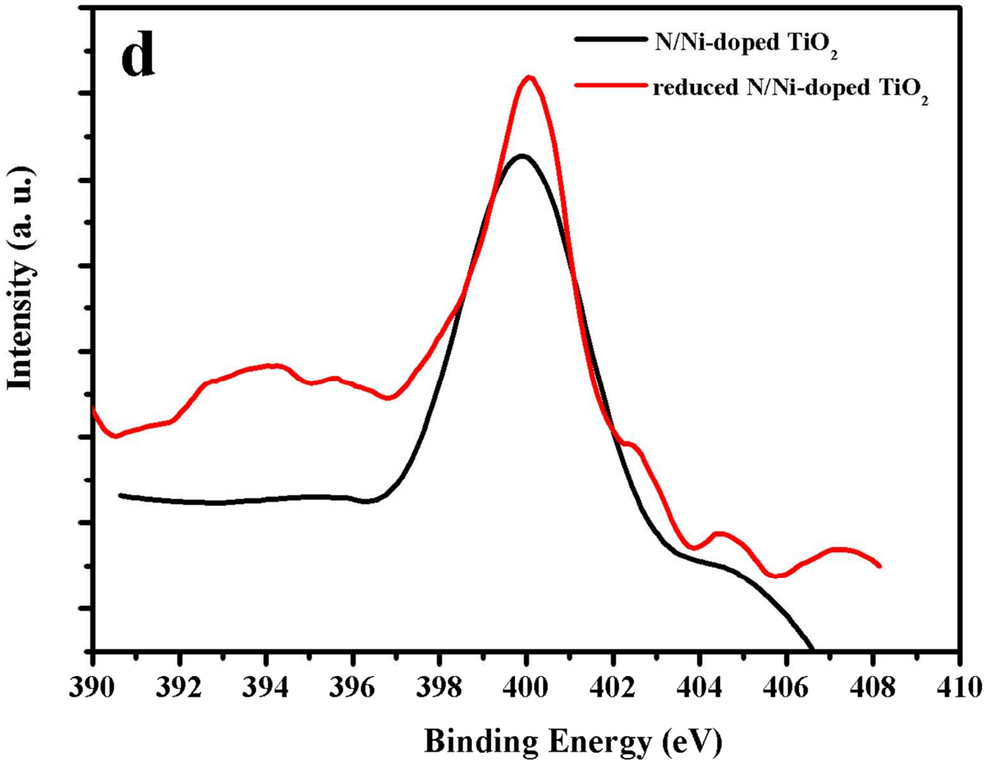

227x178mm (150 x 150 DPI)

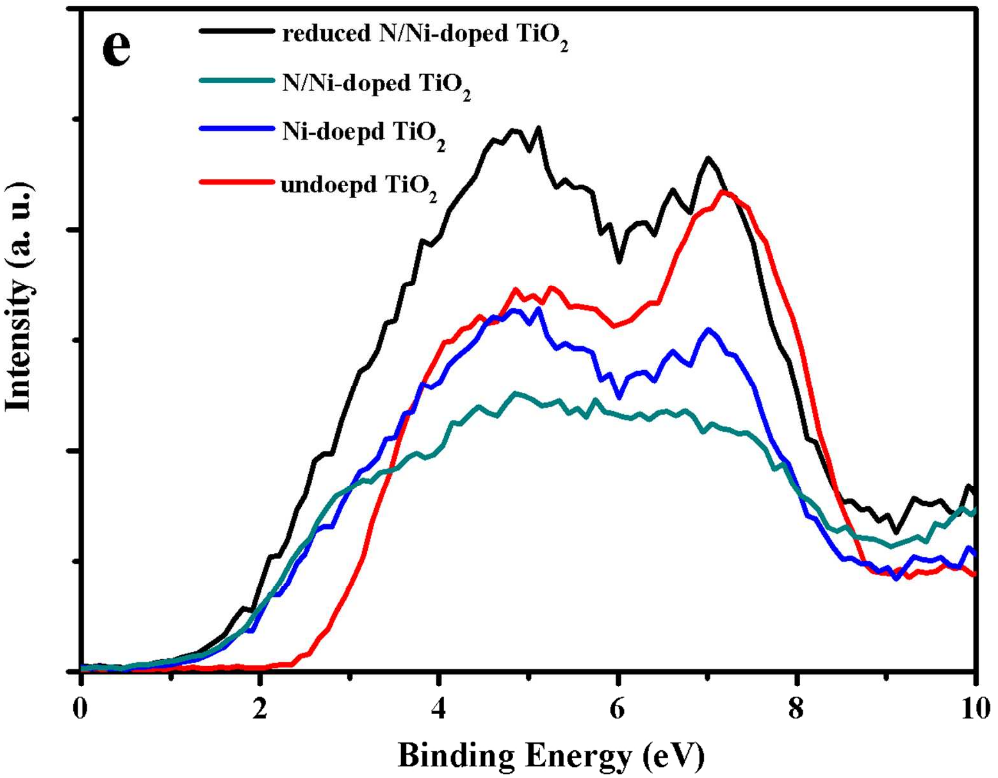

220x176mm (150 x 150 DPI)

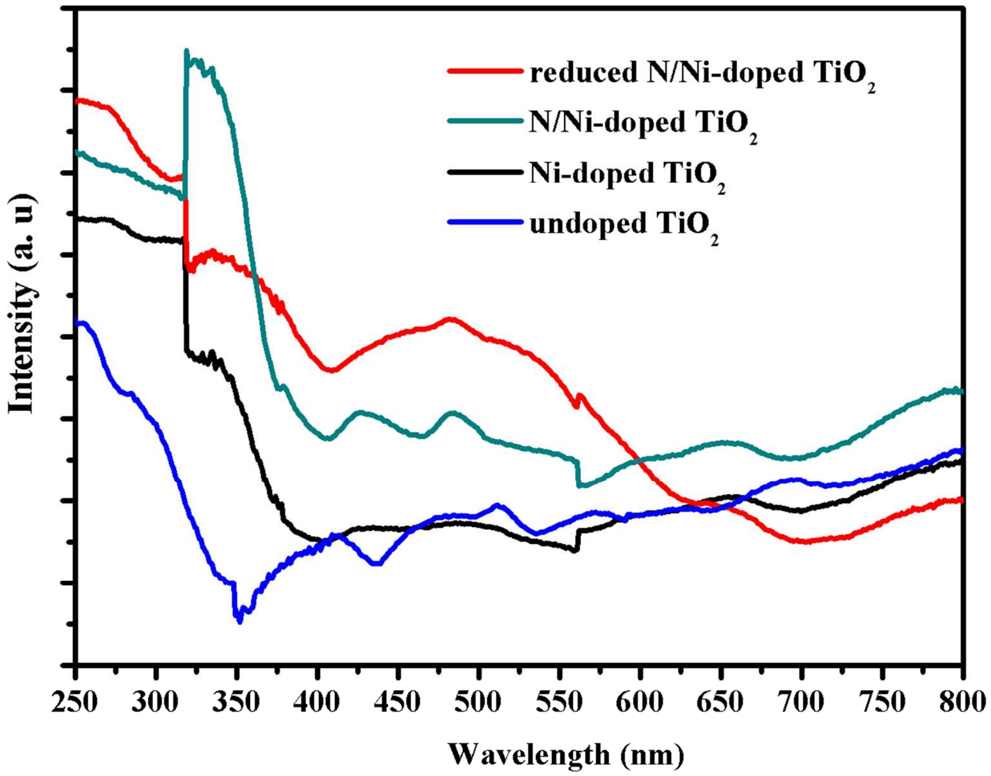

222x176mm (150 x 150 DPI)

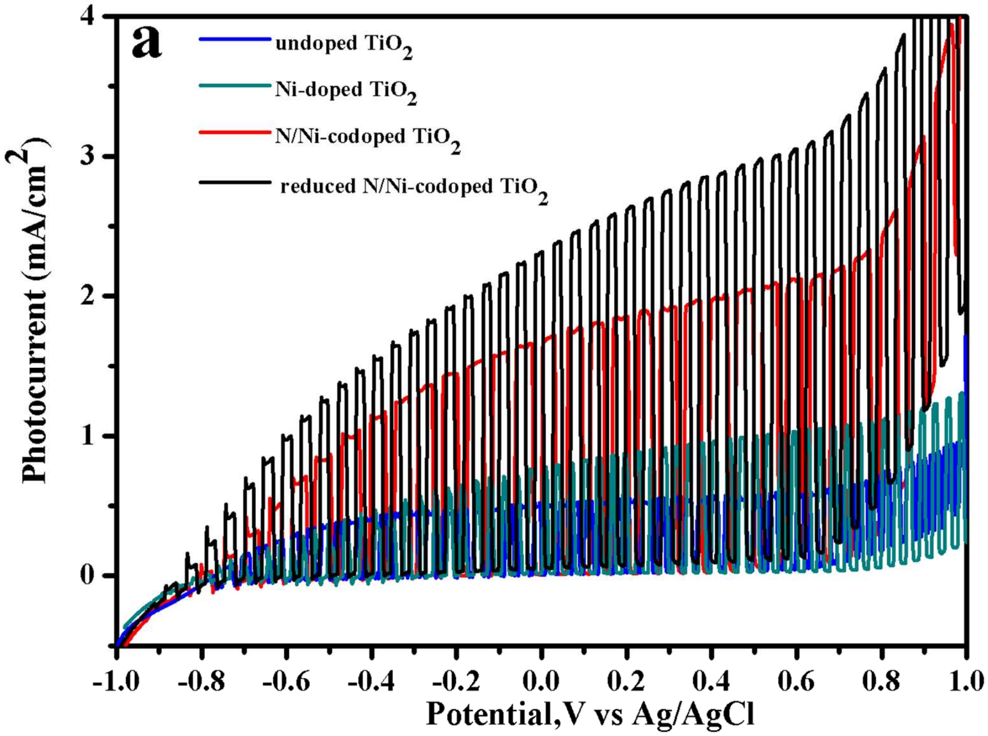

232x177mm (150 x 150 DPI)

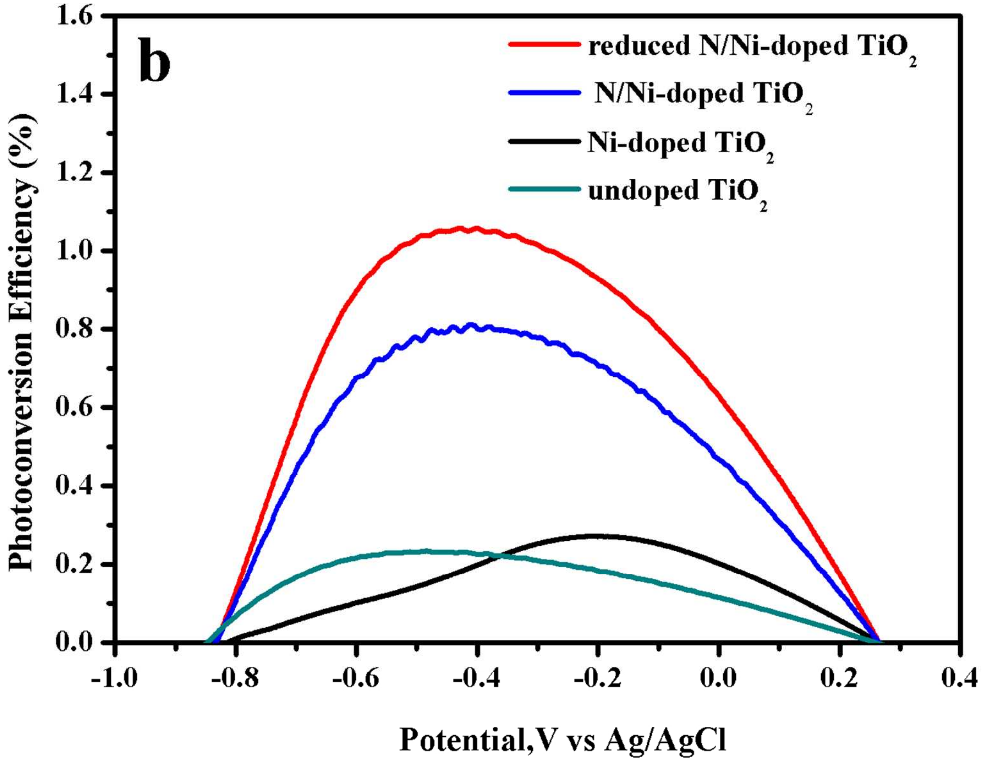

233x183mm (150 x 150 DPI)

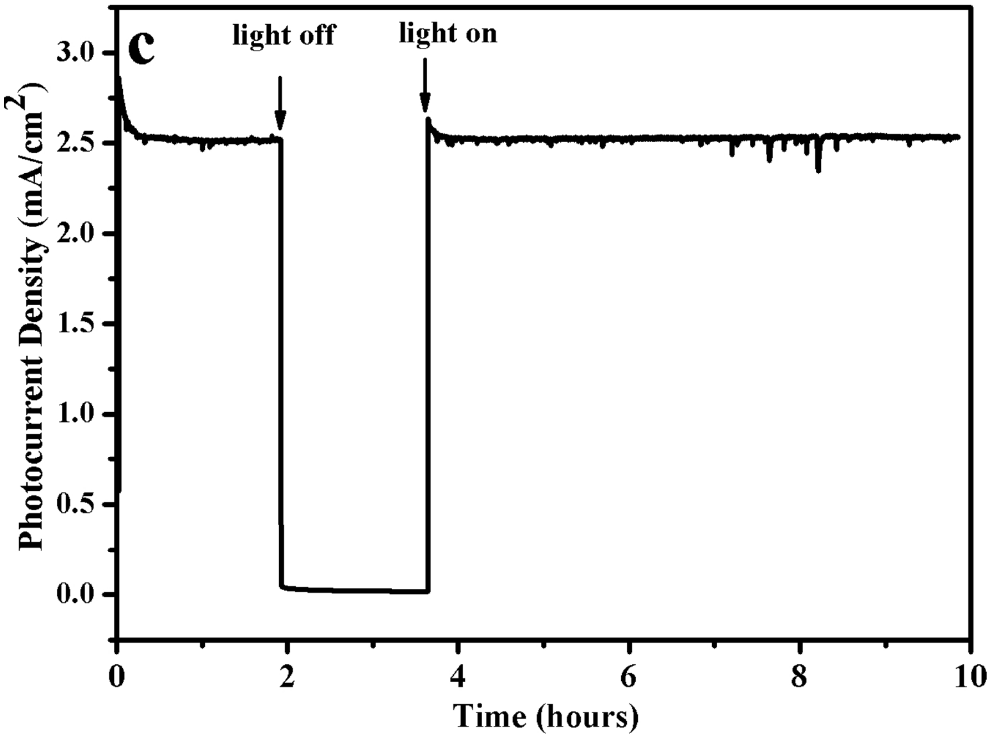

231x174mm (150 x 150 DPI)

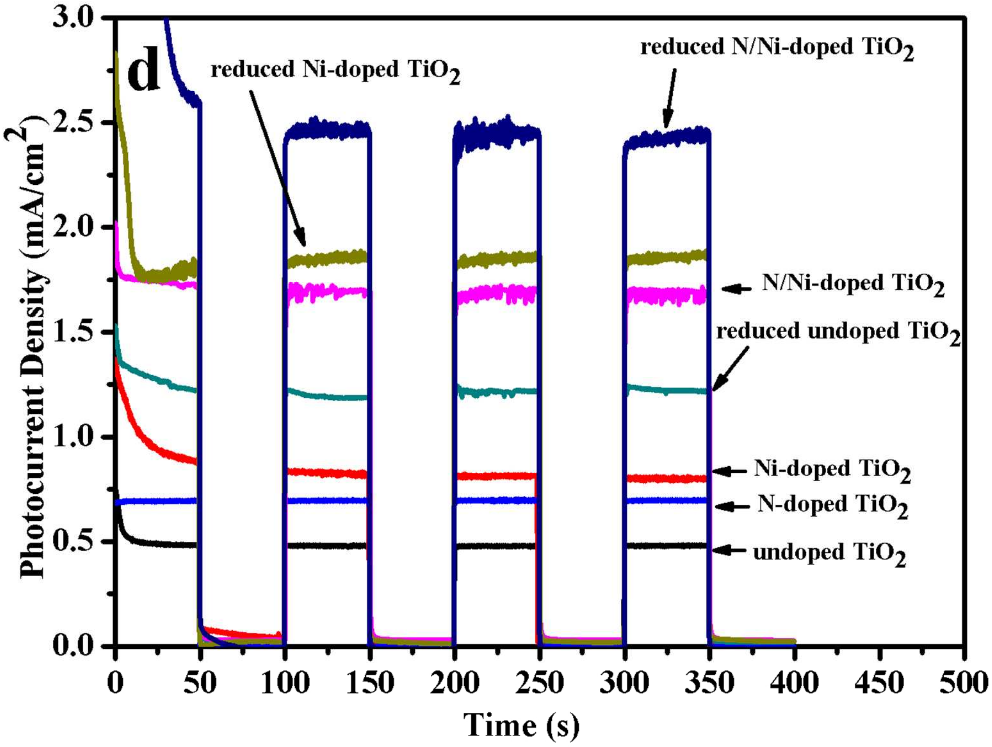

232x176mm (150 x 150 DPI)

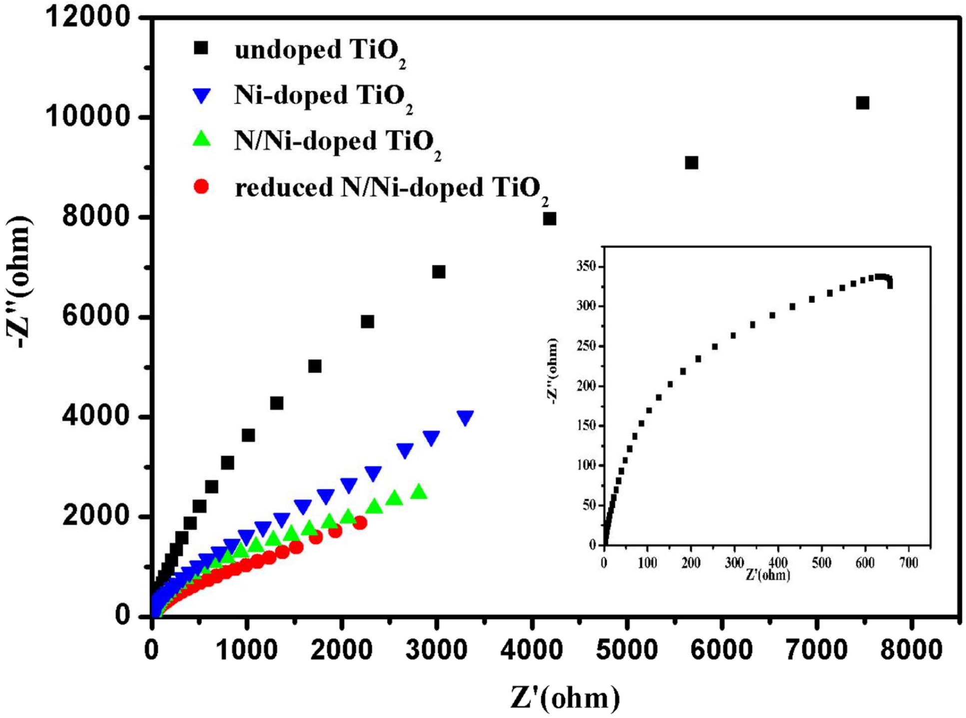

244x180mm (150 x 150 DPI)

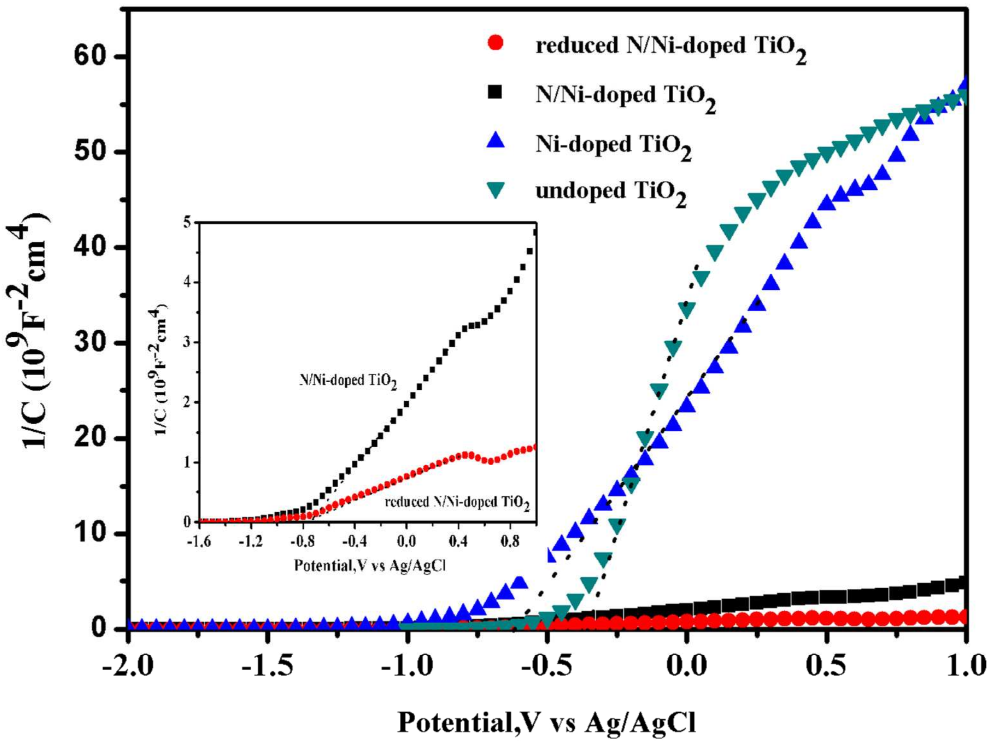

235x179mm (150 x 150 DPI)

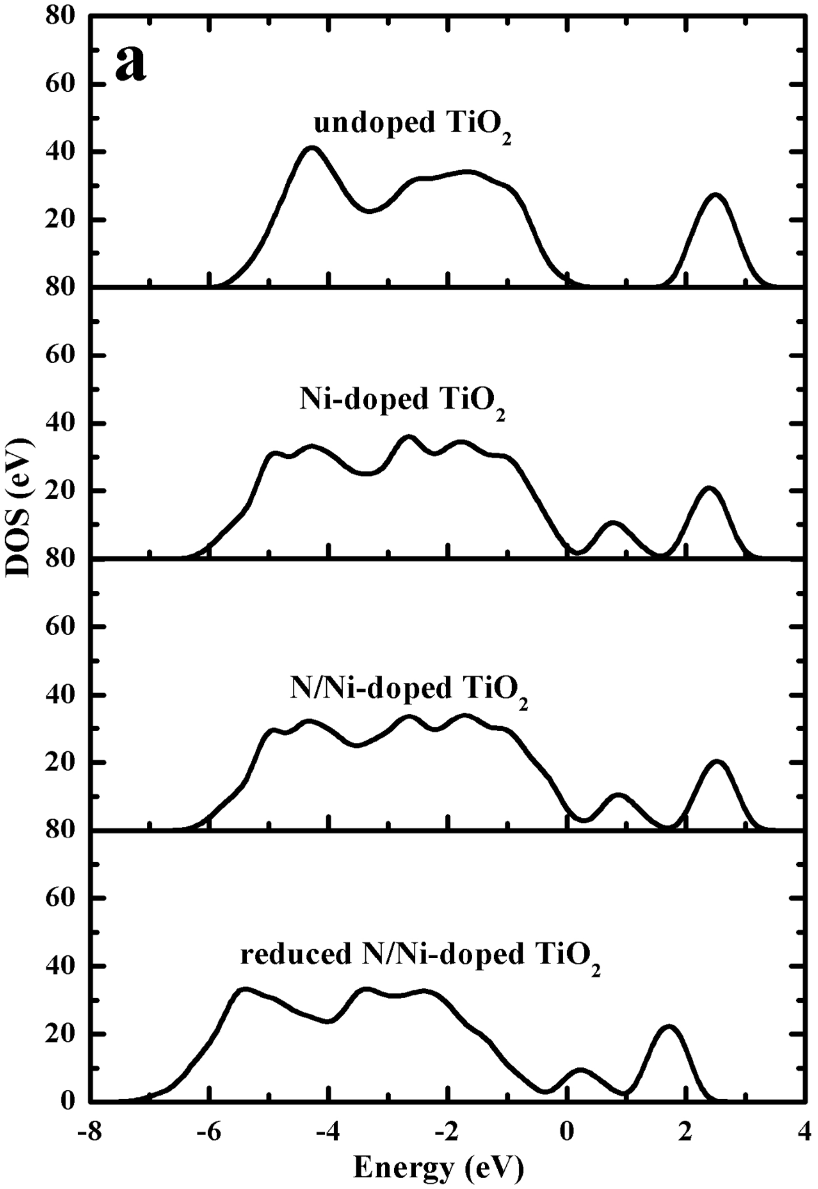

258x363mm (150 x 150 DPI)

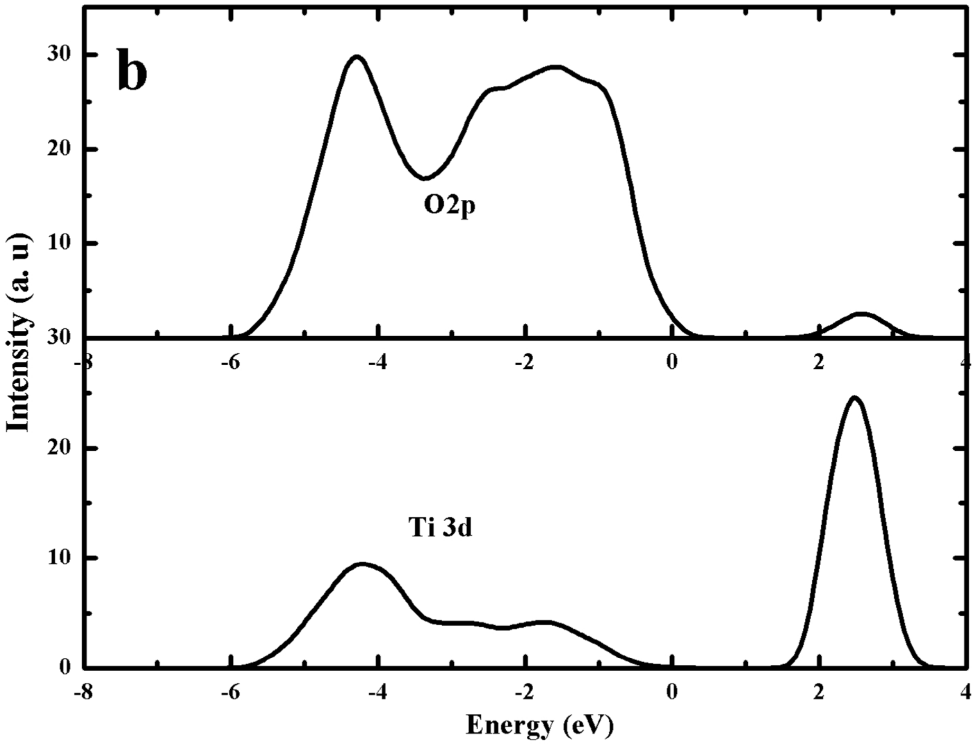

246x187mm (150 x 150 DPI)

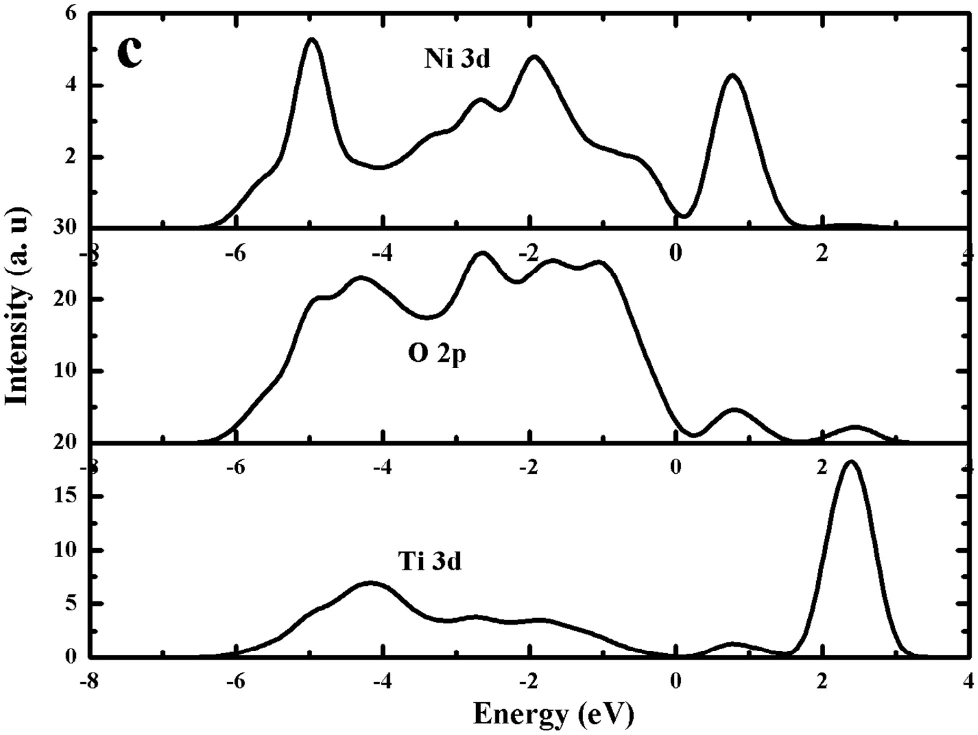

246x186mm (150 x 150 DPI)

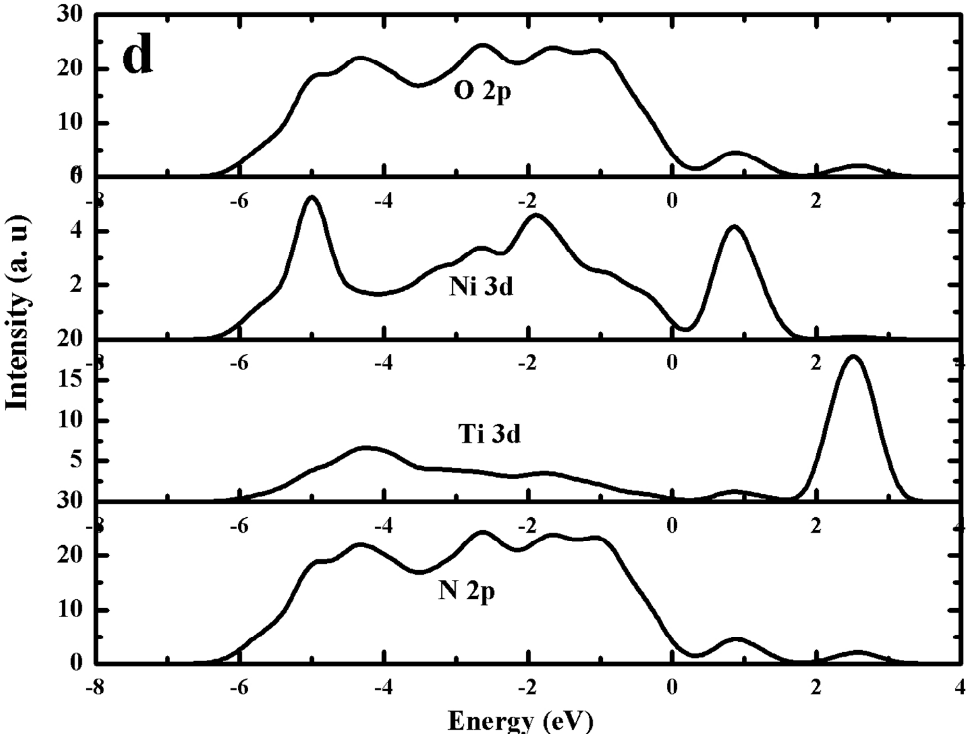

250x193mm (150 x 150 DPI)

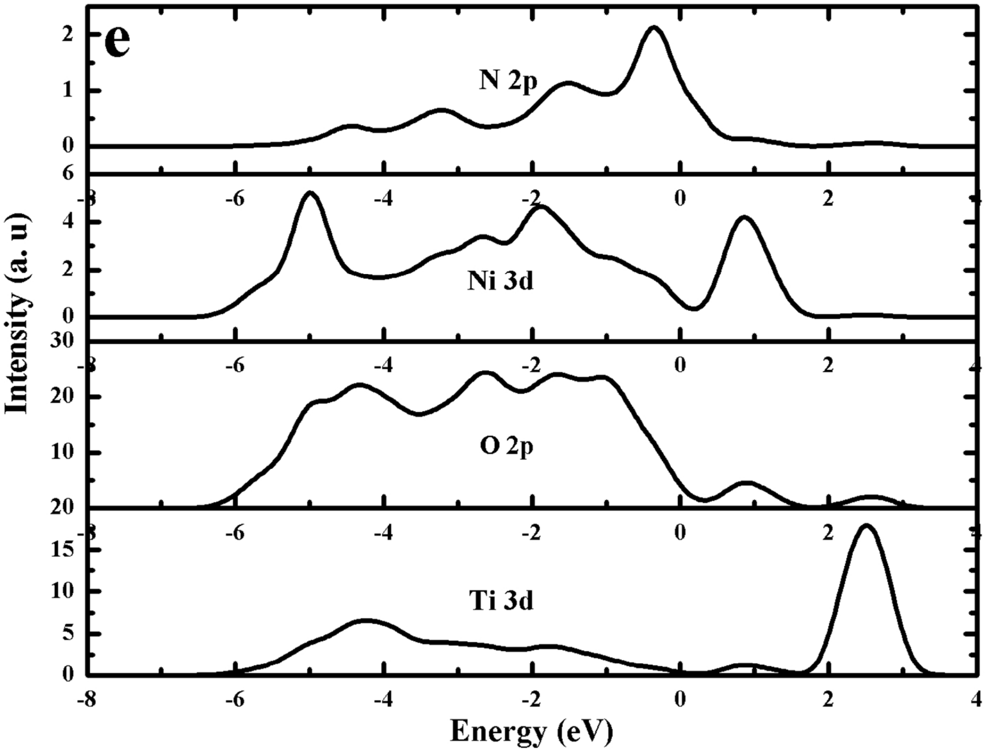

244x189mm (150 x 150 DPI)

Table

Table 1: Flat-band potential (E_{fb}) and donor density (N_d) values obtained from Mott-schottky analysis for different photoanodes.

	undoped TiO_2	**Ni-doped TiO_2**	**N/Ni-doped TiO_2**	**reduced N/Ni-doped TiO_2**
E_{fb}/V	-0.39	-0.64	-0.78	-0.81
N_d/cm^3	9.0×10^{16}	2.1×10^{17}	3.15×10^{18}	7.32×10^{18}

Table 2 Average Mulliken charge on dopant atoms and adjacent atoms of pure, Ni, N/Ni and reduced N/Ni.

	undoped	**Ni-doped**	**N/Ni-doped**	**Reduced N /Ni-doped**
Ti	1.29	-	1.26	1.23
O	-0.65	-0.57	-0.55	-0.58
Ni	-	0.90	0.90	0.87
N	-	-	-0.60	-0.67